Development, Modeling, and Control of a Micro-/Nanopositioning 2-DOF Stick–Slip Device

Micky Rakotondrabe, *Member, IEEE*, Yassine Haddab, and Philippe Lutz, *Member, IEEE*

***Abstract*—The studies presented in this paper are motivated by the high performances required in micromanipulation/microassembly tasks. For that, this paper presents the development, the modeling, and the control of a 2-DOF (in linear and angular motion) micropositioning device. Based on the stick–slip motion principle, the device is characterized by unlimited strokes and submicrometric resolutions. First, experiments were carried out to characterize the performances of the micropositioning device in resolution and speed. After that, a state-space model was developed for the substep functioning. Such functioning is interesting for a highly accurate task like nanopositioning. The model is validated experimentally. Finally, a controller was designed and applied to the micropositioning device. The results show good robustness margins and a response time of the closed-loop system.**

***Index Terms*—Linear and angular motion, micropositioning device, positioning control, state-space modeling, stick–slip.**

I. Introduction

NOWADAYS, the need of miniaturized systems with complex functions is in constant growth. Microfabrication technologies are not always suitable to produce such systems, particularly hybrid systems (i.e., combining several functions: mechanical, electrical, thermal, optical, etc.). For them, microassembly is better adapted. To manipulate and assemble microproducts, especially microelectromechanical systems (MEMS), the use of conventional assembly systems leads to major difficulties because of the scale effects (adhesion forces [1], lack of precision, etc.). In order to take into account these scale effects, a complete study of the actuators, the sensors, and the production methods must be made. Also, production systems should have dimensions that are adapted to those of the products. These systems are called microfactories and consist of microassembly and micromanipulation stations.

As the microcomponents of the microproducts (MEMS, for example) generally have dimensions between 10 μm and 2 mm, it is very interesting to use stations that are able to handle such a range of dimensions. However, a very high positioning accuracy is required in microassembly. It is generally micrometric or submicrometric. So, the positioning devices should have submicrometric resolution. Finally, to pick, transport, and place a component from one location to another in order to complete the assembly, the devices must have a high stroke motion.

For these reasons, a microgripper device with a large gap, high stroke, and high resolution is of interest. Two possibilities may be used.

1) First, one can use a high stroke positioning device coupled with a microgripper [Fig. 1(a)]; examples are provided in [2] and [3]. In order to cover the range of the components sizes, different microgrippers with different gaps are required. The advantage of this solution is that the resolution of the large stroke device does not necessarily have to be very high if the resolution of the microgrippers is. However, a system able to exchange the different microgrippers is required [4].
2) The second solution is the use of two or more independent devices with high stroke that collaborate together in order to pick, transport, and place the components [Fig. 1(b)]. In this case, the gap of the microgripper is naturally unlimited. Two examples of this concept are [5] and [6]. While microgrippers are not necessarily useful, the concept necessitates positioning devices with a high stroke and a high resolution.

As part of our microfactory project, the latter concept was chosen. We describe in this paper the development of a micropositioning device dedicated to a microfactory station. Another important aspect in microassembly is the need of higher

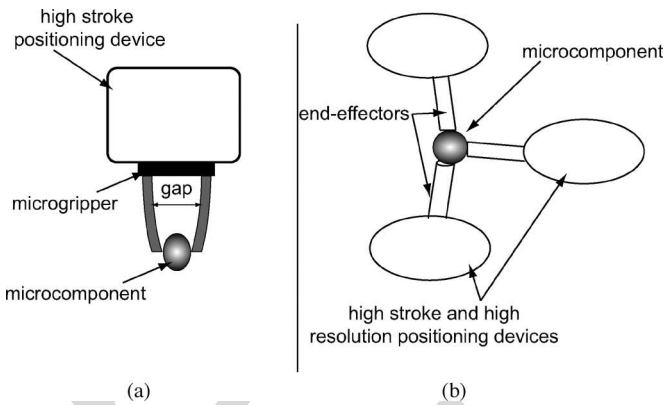

Fig. 1. (a) High stroke positioning device coupled with a microgripper. (b) Several high stroke and high-resolution positioning devices in collaboration.

Manuscript received June 20, 2008; revised October 29, 2008. Recommended by Technical Editor N. Jalili. This work supported in part by the Evolvable Ultra-Precision Assembly SystemS (EUPASS) Project.

The authors are with the Franche-Comté Electronique Mécanique Thermique et Optique–Sciences et Technologies (FEMTO-ST) Institute, Mixed Unit of Research (UMR) National Center for Scientific Research (CNRS) 6174, University of Franche-Comté (UFC)/National School of Mechanics and Microtechnology Besançon (ENSMM)/University of Technology of Belfort-Montbeliard (UTBM), Besançon 25000, France (e-mail: mrakoto@femto-st.fr; yhaddab@ens2m.fr; plutz@femto-st.fr).

Color versions of one or more of the figures in this paper are available online at http://ieeexplore.org.

Digital Object Identifier 10.1109/TMECH.2008.2011134

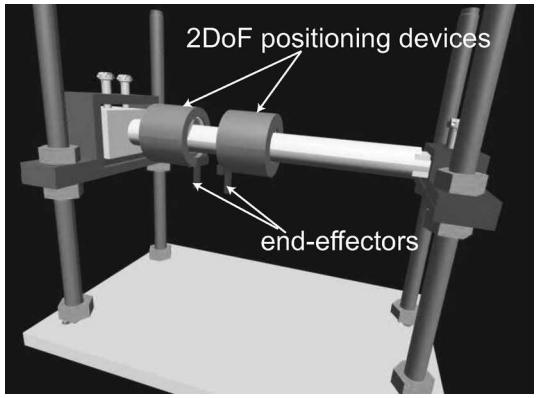

Fig. 2. Principle of the micromanipulation station.

dexterity. As the shapes of the MEMS become more and more complex, positioning devices with a higher number of DOFs are needed. The microrobots presented in [7]–[9] are good examples. Each of them has 3 DOF (x–y linear motions and z angular motion).

On the other hand, the automation of microassembly stations is interesting because the productivity rate can be increased. However, the higher the number of DOF is, the higher the complexity of the automation of positioning devices in collaboration is. A compromise has to be found. We propose the kinematic structure of a microassembly and micromanipulation station, as shown in Fig. 2. The station consists of two devices each having one 2 DOF (linear and angular). One axis supports both the devices in order to increase the ease of their collaboration. This paper reports the development of one 2-DOF micropositioning device based on the stick–slip principle.

When fine positioning is needed in a task, the use of the displacement within a step (substep), i.e., within a stick phase, is preferred. During the fine positioning mode, the disturbances may influence the success of the task. These disturbances may be the variation of the load, the environment (temperature and pressure), etc. In addition, good performances are often necessary for the tasks. They are the response time, the statical error, and the bandpass. To ensure the disturbances rejection and the robustness in performances, a closed-loop control of the positioning device is recommended. Two control modes are also possible for that: the coarse mode control and the fine mode control. For the former, a first approach is the use of a basic algorithm (*if error $>$ one step, then apply a step*) [10]. Another approach is the control of the amplitude of the periodic input signal [11]. Concerning the fine mode, a second-order model and an adaptive sliding mode control is used in [12] to perform while a fourth-order model is obtained in [13] and computes a polynomial digital controller to perform the precise positioning. These controllers are dedicated to only one mode. It is also possible to compute one controller that takes into account both the fine and coarse functioning modes [10], [14]. Notwithstanding, using dedicated controllers remains the best way to obtain good performances because the specifications can be efficiently taken into account during the synthesis. Motivated by the need of high accuracy in micromanipulation/microassembly tasks, we present in this paper the modeling and control of the substep (fine) positioning of the developed micropositioning device.

The paper is organized as follows. First, the development of the micropositioning device is presented. Then, its performances are detailed. After that, a state-space model is developed for the substep functioning. The identification of parameters and the validation of the whole model are presented. Finally, the synthesis and the implementation of a proportional–integral (PI) controller is given. The phase and gain margins of the closed-loop system are high and can ensure the stability and the performances facing the uncertainties on the numerical values of the different parameters of the models.

II. General Description of Micropositioning Device

A. Target System

First, we present the desired characteristics of the microsystem:

1) the device has 2 DOF: linear and angular motions;
2) the desired resolution is greater than 1 μm;
3) in each motion, a very high stroke has to be possible: more than 5 cm in the linear motion and 360° in the angular one;
4) finally, the device has to have adequate dimensions: a maximum volume of $2 \times 2 \times 2$ cm.

B. Presentation of Used Microactuators

There are different principles to obtain the high stroke and the high resolution characteristics of a micropositioning device. They can be classified into principles with embedded microactuators and principles with nonembedded microactuators. It is obvious that those with embedded actuators may offer a theoretically infinite stroke. Among these principles, the stick–slip one is very interesting for two reasons: the compactness of the used microactuators and the simplicity of the control signal (just the use of a sawtooth signal). Stick–slip actuators are generally based on piezoelectric materials. Two modes of motion can be obtained with a micropositioner using stick–slip actuators: the stepping mode and the substep mode. The stepping mode consists of applying a sawtooth voltage to the micropositioner and letting it move step by step, in high range and with a high velocity on the workspace [Fig. 3(a)–(c)]. The resolution in this mode is limited to one step. When the difference between the reference position and the present position becomes smaller than a step, the legs (piezoelectric actuators) are bent slowly until the final position is reached [Fig. 3(d)]. This is the substep mode and the obtained resolution can be very high.

A stick–slip microactuator called *push–pull* microactuator is proposed in [15]. It offers the possibility to perform several DOF from only one bulk material. Due to its characteristics, we use this microactuator in 2-DOF configuration [Fig. 4(a) and (b)] to move our micropositioning device. The microactuator is based on a piezoelectric layer. There are four electrodes on the upper face and one electrode on the electrical ground in the lower face. They constitute the active parts of the microactuator. A sapphire disk-shaped foot is glued on the latter. When a positive electrical potential is applied to two electrodes while

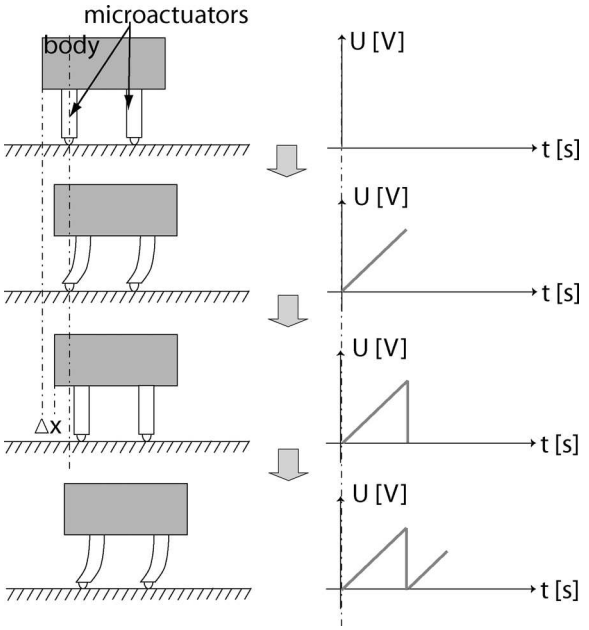

Fig. 3. Stick–slip principle. (a)–(c) Stepping mode. (d) Substep mode.

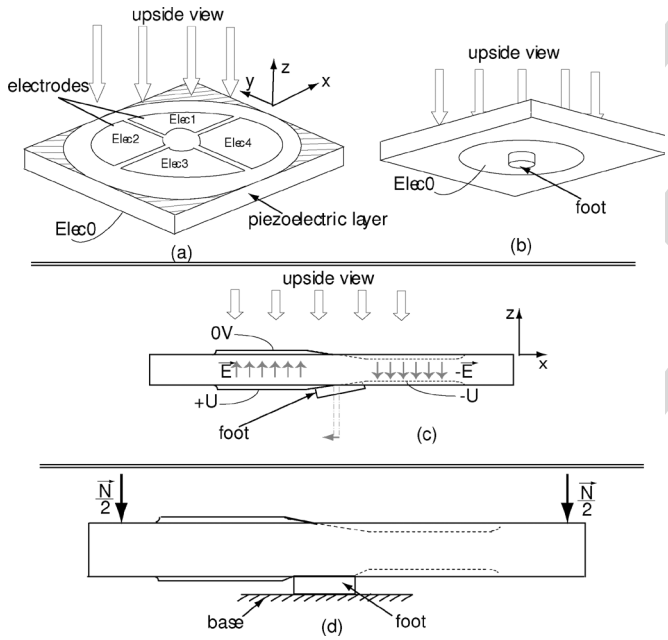

Fig. 4. Push–pull microactuator with 2-DOF configuration [15]. (a) Upside view. (b) Underside view. (c) Displacement and rotation of the foot. (d) Displacement of the microactuator on a base.

the opposite potential is applied to the other two, one-half of the active part contracts while the second one expands. Thus, the foot performs a displacement δ and a rotation [Fig. 4(c)]. Now, let us place the microactuator on a base. If the preload $\vec{N}$ is high enough, there is no rotation of the foot and the displacement of the microactuator only depends on δ [Fig. 4(d)]. The stick–slip motion is obtained when applying a sawtooth voltages to the electrodes. While the foot is in contact with the base, the nonactive surface of the upper face will be glued with the body of the micropositioning device [hatched area in Fig. 4(a)].

C. Integration of Microactuators on 2-DOF Device

This part presents the integration of the aforementioned microactuator inside the 2-DOF device in order to move it. A cylindrical tube is used to support the device. This is the base on which the microactuator will be placed. The upper face of the microactuator is embedded in the device body while the foot is in contact with the tube. We especially use a glass tube because the contact between glass and sapphire materials has optimal friction characteristics.

1) During the stick phase, a sufficient adherence is performed, so the loss of displacement is minimized.
2) During the slip phase, the friction is relatively low, so the issued overheating is minimized. Such overheating may destroy the microactuators elements (sapphire, etc.).

To maintain the axial guidance of the device on the tube, at least two contact points are necessary. However, to maintain the radial guidance, at least three contact points spread out over 360° are necessary. So, we use six contact points to maintain the device on the tube. All the contact points are represented by microactuators in order to obtain a maximal total torque when they are activated simultaneously. The two "axial-guidance" microactuators form a pair of microactuators and glued together on an alumina support in order to facilitate their integration [Fig. 5(a) and (b)]. A system for the adjustment of the radial force is introduced for each pair of microactuators [Fig. 5(c) and (d)]. It is based on two tilted plates (lower and upper) and a screw. Through the plates, the adjustment of the screw will move the microactuator back and forth, and then increases or decreases the radial force. It is used to preload (nominal radial force) the microactuators. However, the glass-tube presents a high cylindricity default and the micropositioning device may work imperfectly. To solve that, the third tilted-plates system is replaced by an adaptable spring system [Fig. 5(e)]. The lateral spring maintains the microactuator pinned against the body while the radial spring compensates the default of the tube. The adaptable springs are built by folding and shearing a thin metallic plate (thickness $= 0.05$ mm) [Fig. 5(f)].

Besides the dimensions, the weight is the main criteria of the design because of the limited torque that the microactuators can deliver. This is why the optimized shape of the body minimizing the weight is a triangle [Fig. 5(b)]. The body is made of alumina material. We call the whole device the triangular RING module (TRING module). Due to the complexity of the shape and the smallness of the dimensions, the body of the TRING module was fabricated with electric-discharge technology. Fig. 6 shows the TRING module on its tube.

III. Characterization of TRING Module

A. Step Characteristics

Here, we evaluate the amplitude of a step of the microsystem in linear and angular motions.

1) Linear Motion: In linear motion, we perform the measurements with an interferometer with a 1.24-nm resolution. Fig. 7(a) shows a linear displacement of the microsystem with a sawtooth voltage with 150 V of amplitude and 500 Hz of

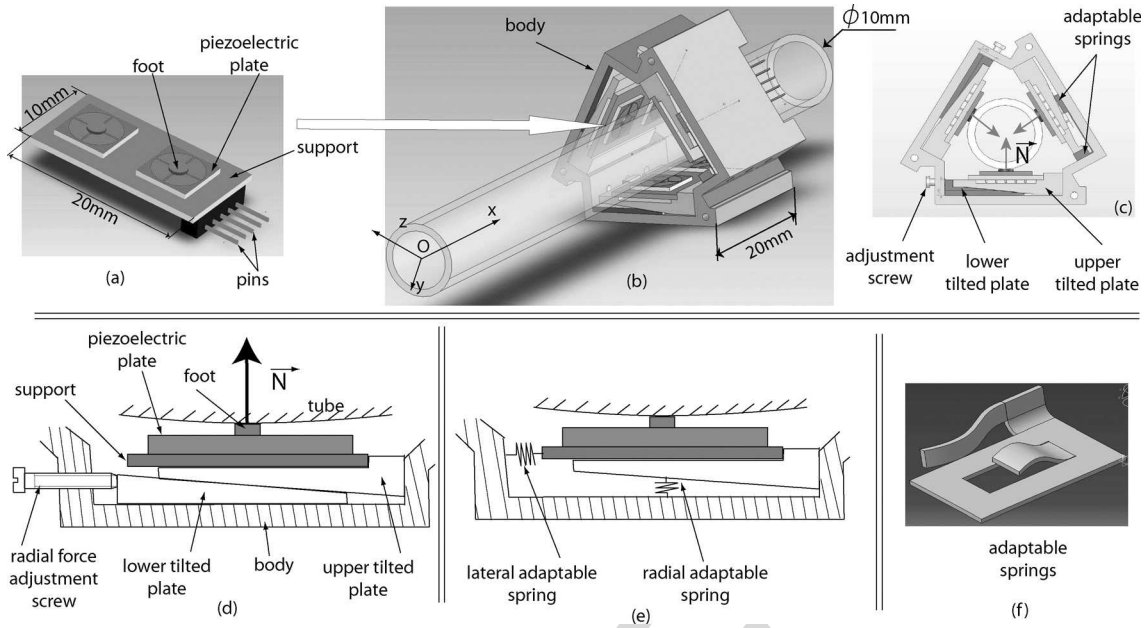

Fig. 5. (a) Pair of microactuators is glued onto a support. (b) and (c) Three pairs of microactuators are spread out inside the device. (d) Tilted-plate system is used to adjust the nominal radial force. (e) and (f) Adaptable spring system is used to compensate the cylindricity defect of the tube.

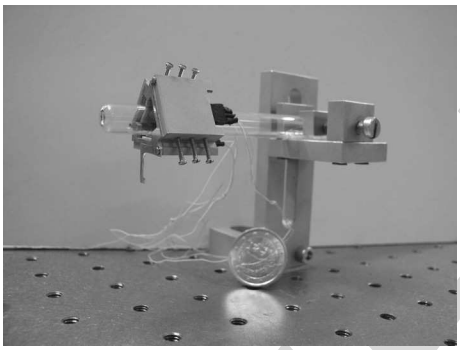

Fig. 6. Photograph of the TRING module on the glass tube.

frequency. We remark that the step is quasi-constant during the displacement. Fig. 7(b) is a zoom of one step. We can note the oscillations during the stick phase caused by the step signal of the previous slip phase. They are due to the dynamic of the microactuators and the mass of the TRING module. The maximal step, obtained with 150 V, is about 200 nm. Decreasing the amplitude will decrease the value of the step and will then increase the resolution of the micropositioning device. As example, with $U = 75$ V, the step is approximatively 70 nm. However, whatever the amplitude is, the step efficiency is constant. The step efficiency is defined as the ratio between the gained step and the amplitude of the applied voltage [16]

$$\eta_{\text{step}} = \frac{\text{step}}{\Delta\text{amp}} \approx 0.7. \quad (1)$$

2) Angular Motion: As we do not have an accurate appropriate sensor to measure the angular motion, we use the linear sensor and apply the measurement principle shown in Fig. 8. Let θ represent the angle of displacement of the microsystem, dl be the tangential displacement, and $R_{\text{meas}} \approx 2$ cm be the radius.

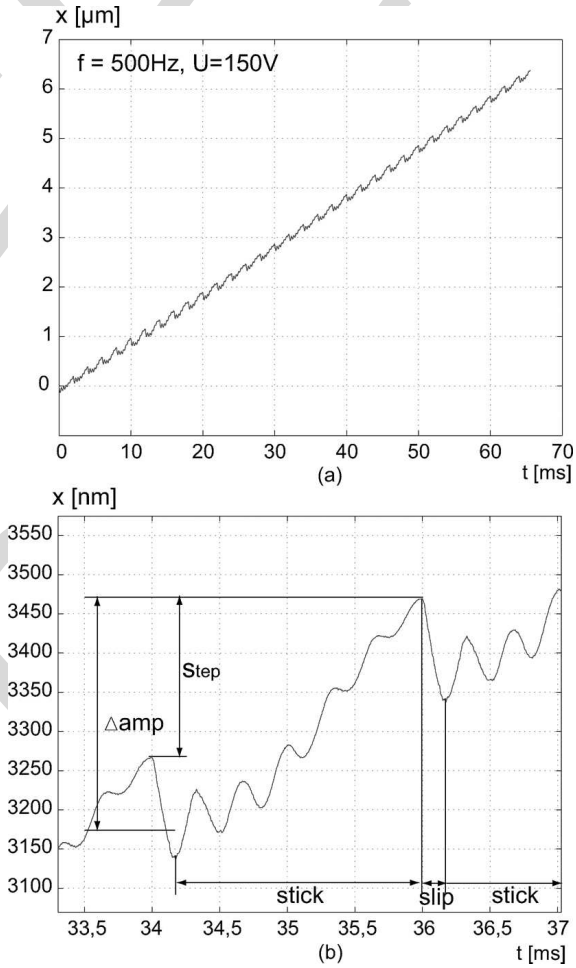

Fig. 7. Linear displacement measurement of the TRING module using an interferometer. (a) Series of stick–slip obtained with $U = 150$ V and $f = 500$ Hz. (b) Vibrations inside a step obtained with $U = 150$ V and $f = 60$ Hz.

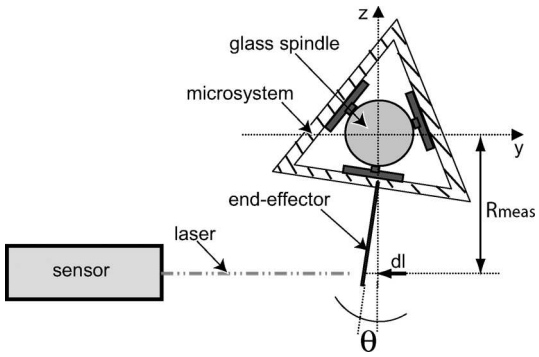

Fig. 8. Principle of measurement during angular motion.

Around the characterization point, we have

$$\theta \approx \frac{dl}{R_{\text{meas}}}. \tag{2}$$

The experiments give a step of 0.0025° with $U = 150$ V, 0.0015° with $U = 100$ V, and 0.001° with $U = 75$ V. Of course, the radius R_{meas} is not exactly known and the used value is approximative. As its uncertainty is bounded by ± 2 cm, the uncertainty on θ is bonded by $\pm 10\%$.

B. High Stroke Characteristics

Here, the capability of the TRING module in terms of speed is analyzed. The analysis is done with different values of frequency and amplitude. To measure the displacement, we use an optical sensor with 500 nm of resolution and ± 4 cm of range for the linear motion while an accelerometer with 1° of accuracy and $\pm 90^\circ$ of range for the angular one is used.

1) Linear Motion: Fig. 9 summarizes the speed performances of the TRING module in linear motion. The spectrum [Fig. 9(a)] indicates the linearity of speed versus frequency (for a given voltage amplitude). Above 10 kHz, saturation and disturbances appear. They are due to the bandpass limit and the eigen frequencies of the microactuators and the entire structure. We can also remark on the linearity of speed versus amplitude (for a given frequency) [Fig. 9(b)]. The applied maximal amplitude is 150 V in order to avoid destruction or depolarization of the piezo microactuators. Below 35 V, the device cannot have a high stroke motion because there is not enough torque to provide the sliding. It only moves back and forth following the microactuators. The maximal speed is about 1.8 mm/s and is obtained when the frequency is 10 kHz and the amplitude 150 V. A test gives the maximal force that the TRING module can deliver. For that, we use a spring with a known stiffness and that is pushed by the device. When the speed of the latter becomes null, the maximal force is obtained: 150 mN. This is good enough for the manipulation of small parts.

2) Angular Motion: To measure angular displacement, we use a capacitive-based sensor from FREESCALE: weight < 2 g, dimensions $2 \times 6 \times 6$ mm. Due to its smallness, it is easily inserted into the TRING module. It has a measurement stroke of $\pm 90^\circ$ and the accuracy depends on the electronic filter and amplifier. As we only take an interest in the high stroke motion, the used accuracy is $\pm 0.5^\circ$. Fig. 10 shows speed performances. The same remarks made about the linear motion can be derived: frequency linearity up to 10 kHz and minimal voltage for displacement about 35 V. Maximal speed is about 20°/s, i.e., nearly 18 s for one complete rotation.

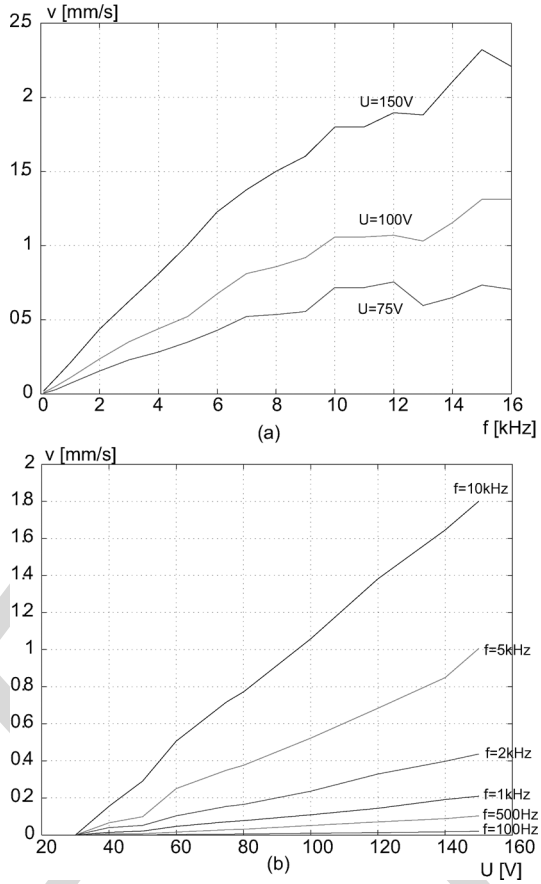

Fig. 9. Speed performances in linear motion.

IV. Substep Modeling of TRING Module

Here, we develop a state-space model of the TRING module working in the substep. There are two reasons why we want to model it: first, to ease the synthesis of a controller, and second, to help the design of the microactuator from given performances.

A. Main Assumptions

The study of the microsystem is reduced to the study of one microactuator with a mass on it. The radial force $\overrightarrow{N}$ applied on each microactuator will be called normal force. The weight of the microsystem is weak in comparison with the result of the normal forces. The manipulation force (load) is not introduced here since it is considered as a disturbance. The adhesion forces between the foot and the spindle are insignificant in relation to the normal force. The base (tube) and the foot are assumed to be rigid and no vibration appears on the tube because we only work in stick phase. During this phase, the foot and the tube are stuck, and then, there is no shock causing any vibration.

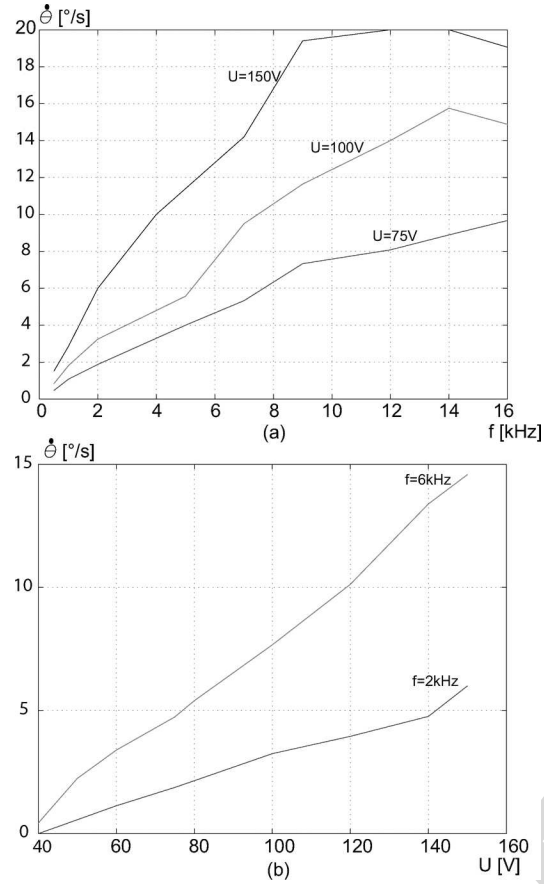

Fig. 10. Speed spectrum in angular motion.

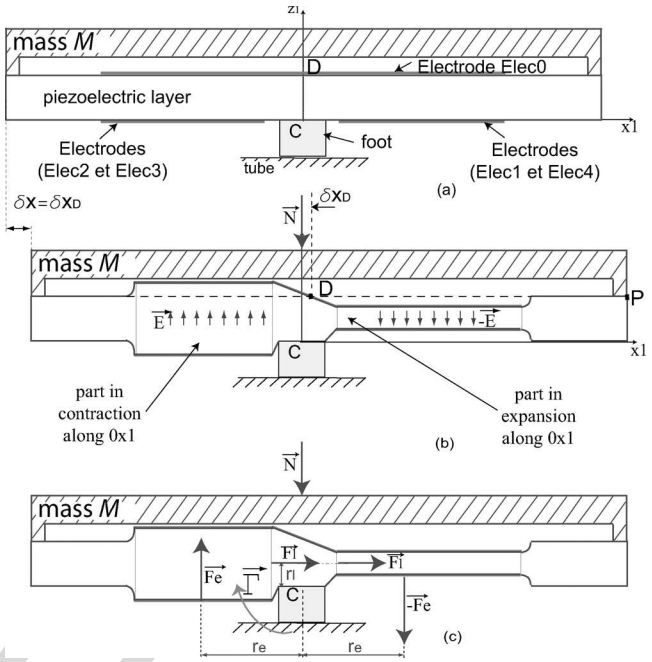

Fig. 11. (a) Mass M is glued on the nonactive area of the microactuator. (b) and (c) Strain of the microactuator.

B. Working Equations

Two parts are considered here: the determination of the piezoelectric working equation and the determination of the friction working equation. The former gives the internal states of the piezoelectric microactuator while the latter gives the internal state of the friction. We will apply the fundamental principle of the dynamics to combine them and obtain the model of the whole device.

1) Piezoelectric Working Equation: Fig. 11(a) shows one microactuator placed on a base. The mass M is composed of the mass of one piezoelectric actuator, one tilted-plate system, and a sixth of the body's mass. Cx_1z_1 represents the local referential in the symmetric plane of the piezoelectric layer. Point C represents the center of the contact surface between the foot and the layer. Point D is the center of the upper surface [Fig. 11(b)]. A displacement δx_D of D generates a displacement δx of the TRING module body with the same amplitude and direction. The aim of this section is to find the displacement of point D relative to point C. When we apply two symmetrical voltages ($+U$ and $-U$) to the electrodes, the piezoelectric layer warps [Fig. 11(b)]. We assume that the radial force $\overrightarrow{N}$ is sufficient to maintain all the lower surface of the foot pinned against the base. Let us isolate the piezoelectric layer. We can summarize the following important parameters [Fig. 11(c)].

1) The resultant force $\overrightarrow{F}$ and the resultant torque $\overrightarrow{\Gamma}$ relative to point C.
2) The scalar fields δx, δy, and δz that, respectively, indicate the displacement fields along Cx_1, Cy_1, and Cz_1 inside the piezoelectric layer. Let δx_D be the value of δx, δy_D the value of δy, and δz_D the value of δz at point D. We assume that δy_D and δz_D are null. Thus, we only focus our study on the evaluation of δx_D.

The resultant force $\overrightarrow{F}$ consists of the following.

1) The normal force $\overrightarrow{N}$. $\overrightarrow{N}$ is assumed to be reduced to point D. When $\delta x_D \neq 0$, we consider that $\overrightarrow{N}$ still stays coaxial with the principal axis of the foot because δx_D is small in relation to the surface.
2) The normal reaction $-\overrightarrow{N}$ applied on point C by the foot to the piezo layer.
3) Two equivalent forces $\overrightarrow{F_e}$ and $-\overrightarrow{F_e}$ are applied to the half active parts of the piezo layer. They are parallel to the electric field. Each of the forces is applied at an equivalent distance r_e from the principal axis. We assume that r_e is constant whatever the strain δx_D is, the latter being negligible compared with the former.
4) A lateral force $\overrightarrow{F_l}$ is applied to each part of the layer. This force is perpendicular to the electric field and is assumed to be at an equivalent distance r_l from the upper surface of the foot. We can consider that r_l is constant whatever the deformation of the piezo layer is because δz_D is null.

The equivalent forces F_e, $-F_e$, and F_l are due to the fact that the foot is constrained in rotation. Foremost, let us study the equation of the two active parts. For that, Sx indicates the contraction (or expansion) of one active part along the Cx_1-axis. In the case of a parallelepipedal layer characterized by a length L, a width w, and a thickness e [Fig. 12(a)], the transversal

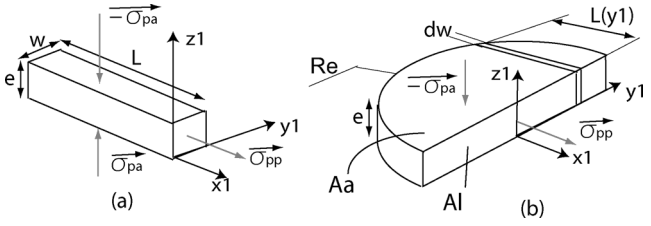

Fig. 12. (a) Parallelepiped piezo layer. (b) Hemicylindrical piezo layer.

strain equation of the piezo layer can be derived using [17]

$$Sx = d_{31}\frac{L}{e}U + s_{13}L\sigma_{pa} + s_{11}L\sigma_{pp} \tag{3}$$

where

1) $d_{31} < 0$, $s_{13} > 0$, and $s_{11} > 0$ are, respectively, the transversal piezoelectric constant, the transversal elastic constant, and the axial elastic constant;
2) σ_{pa} and σ_{pp} represent the mechanical stresses, respectively, parallel and perpendicular to the electrical field, the electrical field being parallel with z_1-axis;
3) e is the thickness at rest (without strain) and $E \approx U/e$.

Notwithstanding, the shape of one active part of the microactuator is not parallelepipedal but hemicylindrical with a radius R_e [Fig. 12(b)]. It can be considered as a sum of parallelepipeds with a constant width dw and a y_1-dependent length written as $L(y_1)$. However, to facilitate the equation of the axial strain Sx, we introduce a shape coefficient c_{oeff} inside (3)

$$Sx = c_{\text{oeff}}\left(d_{31}\frac{R_e}{e}U + s_{13}R_e\sigma_{pa} + s_{11}R_e\sigma_{pp}\right). \tag{4}$$

The previous equation is related to only one active half part. In spite of this, the displacement δx_D can be constructed with the strain of the two half active parts. As the two parts are symmetric, we can use (4) in introducing a correction coefficient c_{orr}. Considering $q = c_{\text{orr}D}\,c_{\text{oeff}}$, we obtain

$$Sx = q\left(d_{31}\frac{R_e}{e}U + s_{13}R_e\sigma_{pa} + s_{11}R_e\sigma_{pp}\right). \tag{5}$$

Let us now evaluate the stresses σ_{pa} and σ_{pp}. Let A_a be the area on which the equivalent force $\overrightarrow{F_e}$ is applied and A_l the area on which the lateral force $\overrightarrow{F_l}$ is applied [Fig. 12(b)]. We have

$$\sigma_{pa} = \frac{F_e}{A_a} \tag{6}$$

$$\sigma_{pp} = \frac{F_l}{A_l}. \tag{7}$$

On the other hand, if we isolate the foot, we have

$$F_{mp} = -2F_l \tag{8}$$

$$\Gamma_{mp} = F_{mp}h_c \tag{9}$$

where F_{mp} and $\Gamma_{mp} = -\Gamma$ are, respectively, the force and the torque applied to the foot by the piezo layer. The height of the foot is represented by h_c. We are reminded that two vertical forces defined by $\overrightarrow{N}$ and $\overrightarrow{-N}$ are also acting on the foot. As their sum equals zero, they will not be considered. Moreover, using a previous assumption stating that $\overrightarrow{N}$ stays coaxial with the foot, the latter force does not influence the torque Γ_{mp}.

Using (5)–(9) and noting that $\delta x = \delta x_D$, we infer

$$\delta x = q\frac{R_e}{e}\left[d_{31}U - ekF_{mp}\right] \tag{10}$$

with

$$k = \frac{h_c s_{13}}{2r_e A_a} + \frac{s_{11}}{2A_l} - \frac{r_l s_{13}}{2r_e A_a}. \tag{11}$$

Equation (10) is a static model. To complete this, we assume that the piezo layer has a second-order dynamic behavior. A higher order would complicate the model, a lower order (first order) is not sufficient if the system has a resonance frequency. If a and b, respectively, represent the inertial and the viscous parameters of the piezo layer, the working equation is

$$\frac{d\dot{\delta}x}{dt} = \frac{qR_e}{ae}\left[d_{31}U - ekF_{mp}\right] - \frac{b}{a}\dot{\delta}x - \frac{1}{a}\delta x. \tag{12}$$

2) Equations of Friction: In the previous part, we determined the displacement of mass M in relation to point C (the foot). In this part, we determine the displacement x_C of point C in relation to the base, and thus to the reference $\Re_0$. In fact, during the stick phase, the predisplacement due to the deflexion of the asperities may have an amplitude with an order of magnitude equivalent to δ_x. In addition, if the state of the friction can be expressed, it will be easy to control the force friction in order to maintain the device working in stick phase. According to the applications, there are several models of friction [18] but the one that allows the modeling of the stick phase is the *single-state elastoplastic model* [19]. The application of this model to our case (stick phase and no lubricant) gives

$$f_f = -N\rho_0 x_C \tag{13}$$

where f_f indicates the deflexion resistance of the medium asperity and ρ_0 represents the Coulomb parameter.

C. State Equations

Here, we write the state equations of the micropositioning device in linear and angular motions. The voltage U is considered as the input variable.

First, let us study the case of linear motion. Fig. 13(a) represents the system when a voltage U is applied. As we only consider the stick phase, we can assume that the reference $\Re_0$ has an origin at the contact between the base and the tip of the medium asperity. In this figure, $\overrightarrow{R}$ is the reaction of the base and is composed of the normal force $-\overrightarrow{N}$ and the tangential force $\overrightarrow{T}$. The latter is the friction. The real system [Fig. 13(a)] can be approximated by Fig. 13(b), where m_p is the mass of the foot and m incorporates the mass M and the mass of the piezo layer. We assume that the point D coincides with the center of the mass m. We also assume that there are no rotation components either for m_p or for m. If we isolate the mass m from the

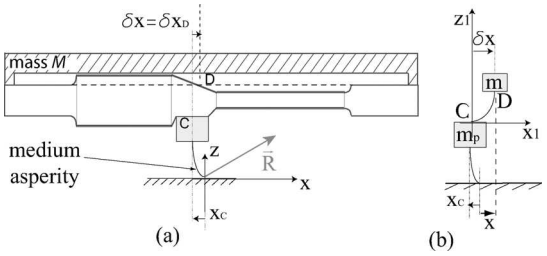

Fig. 13. Scheme of the stick phase. The dimension of asperity is blown up in order to see its deflexion.

precedent remarks and the accelerations law, we have

$$\ddot{x} = \ddot{x}_C + \ddot{\delta}x \tag{14}$$

where x indicates the displacement of the mass m in relation to the reference $\Re_0$. The external forces applied to m are composed of: 1) the force $F_{pm} = -F_{mp}$ applied by the foot and 2) the manipulation force applied by the manipulated component. The latter is assumed to be negligible. If not, it may be considered as an external disturbance. Applying the dynamics law to m and using (14), we can write

$$\ddot{x}_C + \ddot{\delta}x = \frac{-F_{mp}}{m}. \tag{15}$$

On the other hand, isolating the foot lead us to the following dynamics expression:

$$\ddot{x}_C = \frac{1}{m_p}\left(F_{mp} - N\rho_0 x_{as}\right). \tag{16}$$

From the piezo working equation (12), the dynamics of m in (15), and the dynamics of the foot (16), we have the following expressions:

$$\frac{d\dot{\delta}x}{dt} = \frac{1}{m_{equ}}\left(q\frac{R_e}{e}d_{31}U - k_1 x_C - b\dot{\delta}x - \delta x\right) \tag{17}$$

$$\frac{d\dot{x}_C}{dt} = \frac{k_m}{m_{equ}}\left(-q\frac{R_e}{e}d_{31}U + k_2 x_C + b\dot{\delta}x + \delta x\right) \tag{18}$$

with

$$\begin{cases} k_m = \dfrac{m}{(m_p + m)} \\ m_{equ} = a - m_p k_m q R_e k \\ k_1 = k_m q R_e k N \rho_0 \\ k_2 = k_1 - \dfrac{N\rho_0 m_{equ}}{m}. \end{cases} \tag{19}$$

1) State Equation of Linear Mode: Using (17) and (18), we infer the state-space model of the TRING module

$$\frac{d}{dt}\begin{pmatrix} \delta x \\ \dot{\delta}x \\ x_C \\ \dot{x}_C \end{pmatrix} = \begin{pmatrix} 0 & 1 & 0 & 0 \\ -\dfrac{1}{m_{equ}} & -\dfrac{b}{m_{equ}} & -\dfrac{k_1}{m_{equ}} & 0 \\ 0 & 0 & 0 & 1 \\ \dfrac{k_m}{m_{equ}} & \dfrac{bk_m}{m_{equ}} & \dfrac{k_2 k_m}{m_{equ}} & 0 \end{pmatrix}\begin{pmatrix} \delta x \\ \dot{\delta}x \\ x_C \\ \dot{x}_C \end{pmatrix} + \begin{pmatrix} 0 \\ \dfrac{qR_e d_{31}}{em_{equ}} \\ 0 \\ -\dfrac{k_m q R_e d_{31}}{em_{equ}} \end{pmatrix} U. \tag{20}$$

2) State Equation of Angular Mode: Let δs and s_C, respectively, denote the internal state of the piezo layer and the internal state of the medium asperity during the angular mode. As the displacement δs and s_C are very small in relation to the radius of the tube, we can consider that there are no rotation components in the angular mode. The state equation of the two modes are then similar. We have

$$\frac{d}{dt}\begin{pmatrix} \delta s \\ \dot{\delta}s \\ s_C \\ \dot{s}_C \end{pmatrix} = \begin{pmatrix} 0 & 1 & 0 & 0 \\ -\dfrac{1}{m_{equ}} & -\dfrac{b}{m_{equ}} & -\dfrac{k_1}{m_{equ}} & 0 \\ 0 & 0 & 0 & 1 \\ \dfrac{k_m}{m_{equ}} & \dfrac{bk_m}{m_{equ}} & \dfrac{k_2 k_m}{m_{equ}} & 0 \end{pmatrix}\begin{pmatrix} \delta s \\ \dot{\delta}s \\ s_C \\ \dot{s}_C \end{pmatrix} + \begin{pmatrix} 0 \\ \dfrac{qR_e d_{31}}{em_{equ}} \\ 0 \\ -\dfrac{k_m q R_e d_{31}}{em_{equ}} \end{pmatrix} U. \tag{21}$$

D. Output Equations

The output vector has two variables during the stick phase: the total friction T and the displacement x (for the linear motion) or the angle θ (for the angular motion). Indeed, while the displacement is the main interest of the model, in some applications, it is important to estimate or control the friction. For example, if one wants to always ensure the substep functioning mode, the friction T is controlled to be lower than a limit friction such that the stick mode is always guaranteed. If we isolate the foot, we

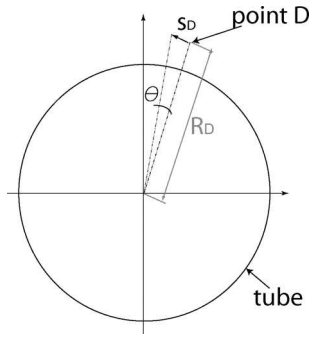

Fig. 14. Angle θ is one of the output variables in the angular mode of the stick phase.

can easily infer that the friction $T = F_{pm}$. To determine this, we use (16).

1) Output Equation of Linear Mode: We have

$$\begin{pmatrix} T \\ x \end{pmatrix} = \begin{pmatrix} -\dfrac{m\,(1-k_m)}{m_{equ}} & -\dfrac{mb\,(1-k_m)}{m_{equ}} & -\dfrac{m\,(k_1-k_2k_m)}{m_{equ}} & 0 \\ 1 & 0 & 1 & 0 \end{pmatrix} \times \begin{pmatrix} \delta x \\ \dot{\delta} x \\ x_C \\ \dot{x}_C \end{pmatrix} + \begin{pmatrix} \dfrac{mqR_e d_{31}\,(1-k_m)}{em_{equ}} \\ 0 \end{pmatrix} U. \tag{22}$$

2) Output Equation of Angular Mode: Fig. 14 represents the simplified scheme of the motion of D in the angular mode. We can approximate $s_D = R_D\theta$, where s_D is the approximated displacement of D ($s_D = \delta s + s_C$) and R_D is the distance between the point D and the spindle axis at rest. Thus, the output equation in the angular mode is

$$\begin{pmatrix} T \\ \theta \end{pmatrix} = \begin{pmatrix} -\dfrac{m\,(1-k_m)}{m_{equ}} & -\dfrac{mb\,(1-k_m)}{m_{equ}} & -\dfrac{m\,(k_1-k_2k_m)}{m_{equ}} & 0 \\ \dfrac{1}{R_D} & 0 & \dfrac{1}{R_D} & 0 \end{pmatrix} \times \begin{pmatrix} \delta s \\ \dot{\delta} s \\ s_C \\ \dot{s}_C \end{pmatrix} + \begin{pmatrix} \dfrac{mqR_e d_{31}\,(1-k_m)}{em_{equ}} \\ 0 \end{pmatrix} U. \tag{23}$$

V. Parameters Identification and Validation of Substep Model

In this section, we identify the unknown parameters of the aforementioned substep modeling. They are the coefficient q and the inertial and the viscous parameters a and b. After identification, we will validate the whole model both for the statical and the dynamical modes. The rest of the parameters are presented in Table I.

TABLE I
Physical and Geometrical Parameters

Dimensions:	
e	$0.5mm$
h_c	$0.5mm$
r_e	$0.5mm$
r_l	$0.25mm$
R_e	$3mm$
gap	$0,2mm$
A_l	$5mm^2$
A_a	$0.367mm^2$
Other parameters:	
d_{31}	$-210 \times 10^{-12} m/V$
s_{11}	$19 \times 10^{-12} m^2/N$
s_{13}	$15 \times 10^{-12} m^2/N$
m	$1g$
m_e	$1.562mg$
ρ_0	$1.583 \times 10^9 m^{-1}$
N	$1N$

Due to the lack of an accurate angular sensor, we only process the linear motion mode. This does not allow a loss of generality because the angular motion model has the same parameters as the linear motion model except the radius of the tube. We use an interferometer of 1.24 nm resolution for the experiments.

Using the state-space equation (20) and the output equation (22), we derive the transfer function relating the substep displacement x and the voltage U

$$G_{xU} = \frac{x(s)}{U(s)} = \frac{qR_e d_{31}}{e} \frac{\left(b_2^{num} s^2 + 1\right)}{\left(a_4^{den} s^4 + a_3^{den} s^3 + a_2^{den} s^2 + a_1^{den} s + 1\right)} \tag{24}$$

with

$$\begin{cases} b_2^{num} = \dfrac{m_{equ}}{k_m\,(k_1-k_2)} \\ a_4^{den} = \dfrac{m_{equ}^2}{k_m\,(k_1-k_2)} \\ a_3^{den} = \dfrac{bm_{equ}}{k_m\,(k_1-k_2)} \\ a_2^{den} = \dfrac{m_{equ}\,(1-k_2k_m)}{k_m\,(k_1-k_2)} \\ a_1^{den} = b \end{cases}. \tag{25}$$

In addition to the parameters identification, the transfer function described in (24) will be used to synthesize a controller in the next section.

A. Identification of Parameter q

The steady-state form of the transfer function (24) is

$$q = \frac{xe}{d_{31} R_e U}. \tag{26}$$

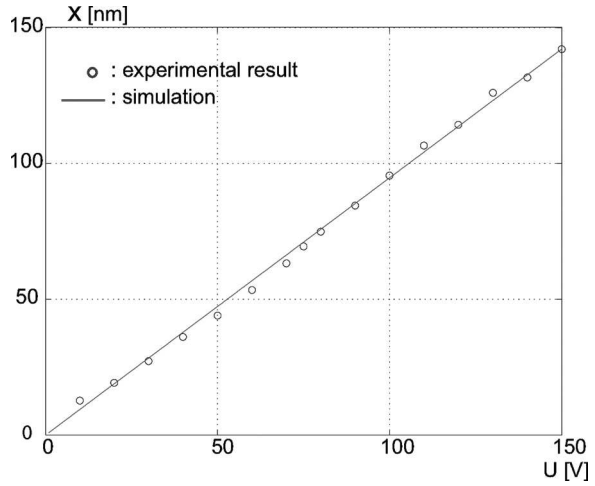

Fig. 15. Validation of the static regime and the identified parameter q.

On the other hand, when the steady state is reached, the deflection of the medium asperity becomes null. Thus, to determine q, a statical analysis with a piezoelectric actuator can be performed. Considering the smallness of the piezo layer, it is impossible to isolate it and to carry out experiments. A statical analysis with a finite-element method (FEM) method (with ANSYS) was then performed. We apply a voltage of 150 V. The corresponding displacement is $x = 142$ nm. Thus, we have $q = 0.7515$.

B. Validation of Steady-State Model

To validate the structure of the steady-state equation (26) and the determined value of q, we compare the corresponding simulation with an experimental result for different values of U. Fig. 15 shows that the curves align well.

C. Identification of Parameters a and b

Considering the smallness of the piezo layer, it is impossible to isolate them and determine the parameters a and b. Thus, we perform a harmonic analysis of one microactuator with an FEM method (with ANSYS). We obtain $a = 9.77 \times 10^{-10}$ s^2 and $b = 200 \times 10^{-6}$ s.

D. Validation of Whole Model

To validate the whole model (24) with the different identified parameters, we use a harmonic experimental analysis of the TRING module. The chosen amplitude of the sine voltage is 75 V instead of 150 V. Indeed, with a high amplitude, the minimum frequency from which the drift starts is low. In the example of Fig. 16, a frequency of 2250 Hz already derives a drift when the amplitude is 150 V while a frequency of 5000 Hz does not when it is 75 V. The higher the amplitude is, the higher the acceleration is, and consequently, the higher the risk of sliding (drift) is. When the TRING module slides, the substep model is no longer valid. Fig. 17 presents the magnitude of the simulation of (24) and the experimental result. It shows that the structure of the model and the identified parameters are befitting.

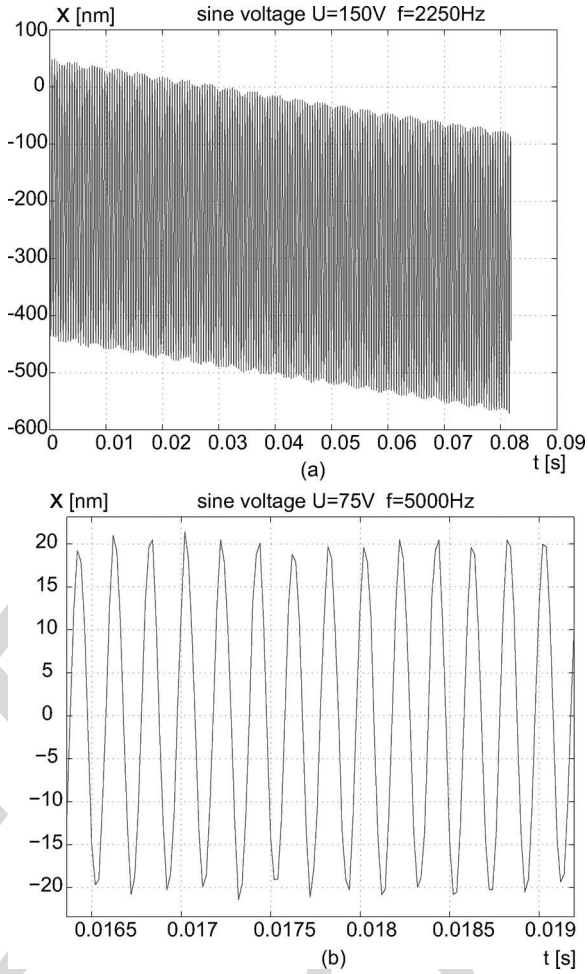

Fig. 16. Outbreak of a drift of the TRING module happens at low frequency when the amplitude is high.

VI. Control of Substep Functioning

The aim of the substep control is to improve the performances of the TRING module during a high accurate task and to reject the disturbances (manipulation force, adhesion forces, and environment). Indeed, when positioning a microcomponent, the manipulation force can disturb the positioning task and modify its accuracy. In addition, the numerical values of the parameters (physical and geometrical) are uncertain. Thus, we want to introduce high stability margins in the closed-loop system.

The substep functioning necessitates that the derivate of the voltage dU/dt should be inferior to a maximum slope $\dot{U}_{\max}$. A rate limiter is then introduced in the closed-loop scheme in order to limit the slope of U [Fig. 18(a)].

A proportional controller was first applied. Due to the non-negligible statical error, an integrator was afterwards added. For the closed-loop system, we want to have a phase margin of 60°. To calculate the corresponding proportional gain K_p and integrator gain $K_i = 1/T_i$ (T_i is the integrator time parameter), we trace the Black–Nichols diagram of the open-loop system G_{xU} (Fig. 19). Let $K_{\mathrm{PI}} = K_p\,(1 + K_i(1/s))$ be the transfer function of the controller. The margin phase of 60° is obtained if the new open-loop transfer function $K_{\mathrm{PI}}G_{xU}$ has a Black–Nichols

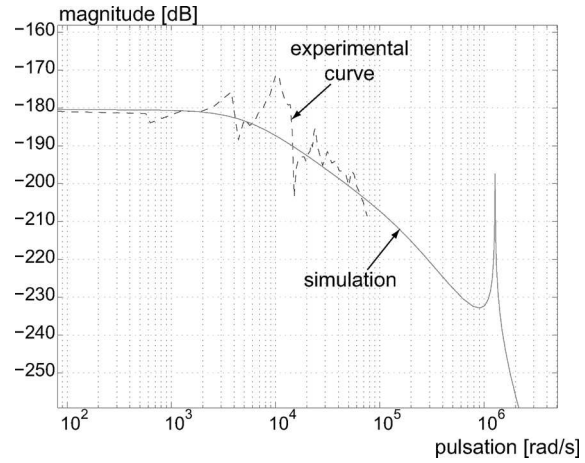

Fig. 17. Validation of the complete model.

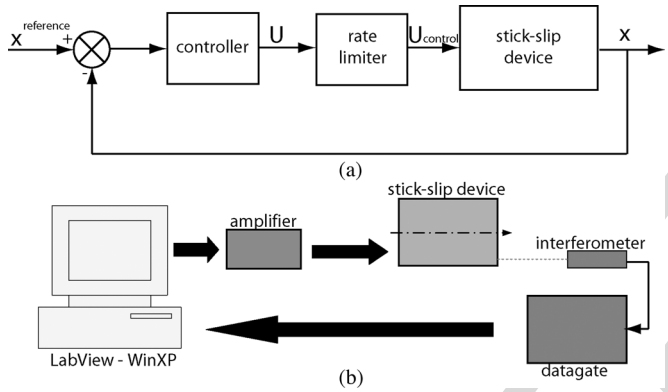

Fig. 18. (a) Structure of the closed-loop system. (b) Setup structure.

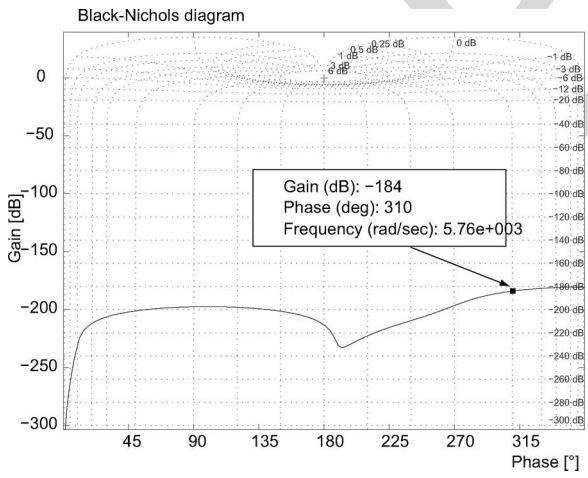

Fig. 19. Black–Nichols diagram of G_{xU}.

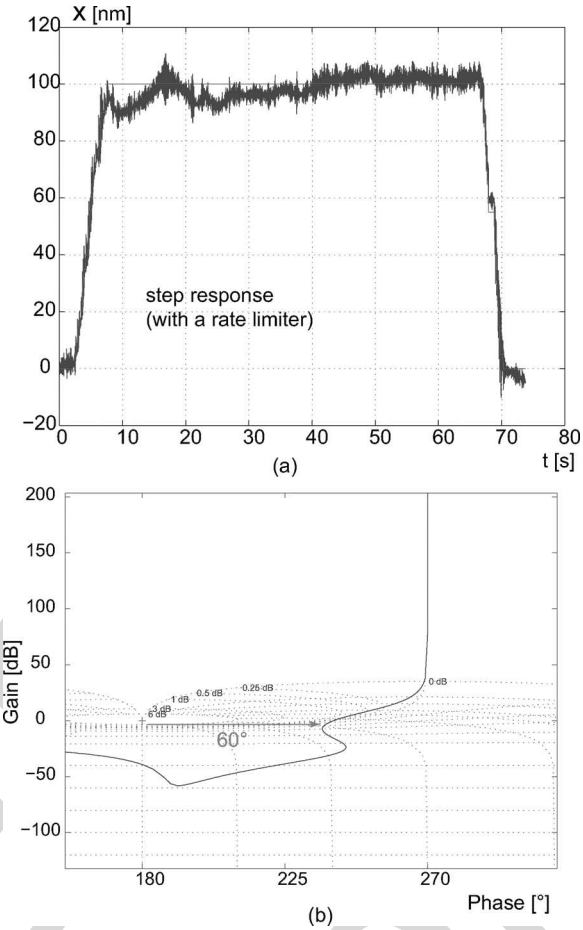

Fig. 20. PI control of the TRING module in substep functioning.

diagram that cuts the 0 dB horizontal axis at $240°$. The goal is then to compute a corrector K_{PI} that moves the diagram of Fig. 19 up to the desired diagram. For that, we choose a point of the initial diagram and move it up to the point $(0\ \mathrm{dB}, 240°)$. As the integrator provides a delay, the chosen point should have a phase that is more than $240°$. We take $(-184\ \mathrm{dB}, 310°)$ (Fig. 19).

This point is obtained with a frequency of $\omega_0 = 2.89 \times 10^3$ rad/s. After that, two operations are applied.

1) Addition of a gain of 184 dB. The corresponding ratio is $g_K = 1\,122\,018\,454$.
2) Application of the phase delay due to the integrator: $\varphi_i = 310° - 240° = 70°$.

From these data, we have

$$T_i = \frac{1}{\omega_0 \tan(\varphi_i)} = 125.94 \times 10^{-6} \tag{27}$$

$$\gamma = \frac{T i \omega_0}{\sqrt{1 + (T i \omega_0)^2}} = 0.3420 \tag{28}$$

where γ is the gain at high frequency. We directly infer

$$K_p = \gamma g_{\mathrm{K}} = 383\,749\,529 \tag{29}$$

$$K_i = \frac{1}{T_i} = 7940. \tag{30}$$

The controller was implemented following the principle scheme in Fig. 18. The reference displacement is a step input signal $x^{\mathrm{reference}} = 100$ nm. Because the voltage generated by the controller is rate-limited, the settling time relative to the step input is no more of great interest. Hence, we are more interested by the static precision. Fig. 20(a) shows the experimental

response of the TRING module. The accuracy is about ± 5 nm and the vibrations are due to the high sensitivity of the measurement to the environment. Such performances are of great interest for micromanipulation/microassembly. Fig. 20(b) shows the Black–Nichols diagram of the closed-loop system and indicates the margin phase. According to the figure, the margin gain is 50 dB. These robustness margins are widely sufficient to ensure the stability of the closed-loop system regarding the uncertainty of the parameters and the structure of the developed model. Finally, the interest of the closed-loop control is to ensure these performances when external disturbances will appear during the micromanipulation/microassembly tasks. It may concern the environmental disturbance (temperature variation, etc.) or the manipulation disturbance (manipulation force).

VII. Conclusion

In this paper, we have presented the development, the substep modeling, and control of a 2-DOF (linear angular) micropositioning device, named TRING module.

The device is based on the stick–slip principle that enables it to have submicrometric resolution and large strokes. The performance analysis shows that the TRING module is well suited for the automated microassembly stations. These performances concern the strokes, the high accuracy, and the speeds. Moreover, in order to improve the performances in nanopositioning, we have developed a state-space model of the substep of the device working within a step. The model has been experimentally validated. Finally, we have implemented a PI controller making the substep mode have good performances for micromanipulation and microassembly use and a good robustness facing an eventual uncertainty of the parameters of the model.

Acknowledgment

The authors would like to thank Dr. J.-M. Breguet from the Laboratoire des Systèmes Robotiques of the Swiss Federal Institute of Technology Lausanne (LSRO-EPFL), for providing us the microatuators, sensors, and advice.

References

[1] R. S. Fearing, "Survey of sticking effect for micro parts handling," in *Proc. IEEE Int. Conf. Intell. Robots Syst. (IROS)*, Pittsburgh, PA, 1995, vol. 2, pp. 212–227.

[2] Q. Zhou, A. Aurelian, C. del Corral, P. J. Esteban, P. Kallio, B. Chang, and K. N. Koivo, "A microassembly station with controlled environment," *Proc. SPIE*, vol. 4568, pp. 252–260, 2001.

[3] N. Dechev, L. Ren, W. Liu, W. L. Cleghom, and J. K. Mills, "Development of a 6 degree of freedom robotic micromanipulator for use in 3D MEMS microassembly," in *Proc. IEEE Int. Conf. Robot. Autom. (ICRA)*, Orlando, FL, May 2006, pp. 281–288.

[4] C. Clévy, A. Hubert, and N. Chaillet, "A new micro-tools exchange principle for micromanipulation," in *Proc. IEEE Int. Conf. Intell. Robots Syst. (IROS)*, Sendai, Japan, Sep. 28–Oct. 2, 2004, pp. 230–235.

[5] J. A. Thompson and R. S. Fearing, "Automating microassembly with orthotweezers and force sensing," in *Proc. IEEE Int. Conf. Intell. Robots Syst. (IROS)*, Maui, HI, Nov. 2001, vol. 3, pp. 1327–1334.

[6] W. Driesen, T. Varidel, and S. Régnier, J. M. Breguet, "Micro manipulating by adhesion with two collaborating mobile micro robots," *J. Micromech. Microeng.*, vol. 15, no. 10, pp. S259–S267, 2005.

[7] S. Fatikow, B. Magnussen, and U. Rembold, "A piezoelectric mobile robot for handling of microobjects," in *Proc. Int. Symp. Microsyst., Intell. Mater. Robots*, Sendai, Japan, 1995, pp. 189–192.

[8] A. Kortschack, O. C. Hanbler, C. Rass, and S. Fatikow, "Driving principles of mobile microrobots for the micro- and nanohandling," in *Proc. IEEE Int. Conf. Intell. Robots Syst. (IROS)*, Las Vegas, NV, Oct. 27–31, 2003, pp. 1895–1900.

[9] A. Bergander, W. Driesen, T. Varidel, M. Meizoso, and J. M. Breguet, "Mobile $cm3$-microrobots with tools for nanoscale imaging and micromanipulation," in *Proc. Mechatronics Robot. (MechRob 2004)*, Aachen, Germany, Sep. 13–15, pp. 1041–1047.

[10] M. Rakotondrabe, Y. Haddab, and P. Lutz, "Voltage/frequency proportional control of stick-slip micropositioning systems," *IEEE Trans. Control Syst. Technol.*, to be published.

[11] S. Fatikow, T. Wich, H. Hülsen, T. Sievers, and M. Jähnisch, "Microrobot system for automatic nanohandling inside a scanning electron microscope," *IEEE/ASME Trans. Mechatronics*, vol. 12, no. 3, pp. 244–252, Jun. 2007.

[12] S. K. Hung, E. T. Hwu, M. Y. Chen, and L. C. Fu, "Dual-stage piezoelectric nano-positioner utilizing a range-extended optical fiber Fabry–Perot interferometer," *IEEE/ASME Trans. Mechatronics*, vol. 12, no. 3, pp. 291–298, Jun. 2007.

[13] S. P. Salisbury, D. F. Waechter, R. B. Mrad, S. E. Prasad, R. G. Blacow, and B. Yab, "Closed-loop control of a complementary clamp piezoworm actuator," *IEEE/ASME Trans. Mechatronics*, vol. 12, no. 6, pp. 590–598, Dec. 2007.

[14] B. Sedghi, "Control design of hybrid systems via dehybridization," Ph.D. dissertation, Ecole Polytech. Fédérale de Lausanne, Lausanne, Switzerland, 2003.

[15] A. Bergander, W. Driesen, T. Varidel, and J. M. Breguet, "Monolithic piezoelectric push-pull actuators for inertial drives," in *Proc. IEEE Int. Symp. Micromechatronics Hum. Sci.*, Oct.19–22, 2003, pp. 309–316.

[16] W. Driesen, A. Bergander, T. Varidel, and J. M. Breguet, "Energy consumption of piezoelectric actuators for inertial drives," in *Proc. IEEE Int. Symp. Micromechatronics Hum. Sci.*, Oct.19–22, 2003, pp. 51–58.

[17] *An American National Standard—IEEE Standard on Piezoelectricity*, ANSI/IEEE, 1987.

[18] B. Armstrong-Hélouvry, P. Dupont and C. Canudas-De Wit, "A survey of models, analysis tools and compensation methods for the control of machines with friction," *Automatica*, vol. 30, no. 7, pp. 1083–1138, 1994.

[19] P. Dupont, V. Hayward, B. Armstrong, and F. Altpeter, "Single state elastoplastic models," *IEEE Trans. Autom. Control*, vol. 47, no. 5, pp. 787–792, May 2002.

[20] M. Rakotondrabe, Y. Haddab, and P. Lutz, "Design, development and experiments of a high stroke-precision 2DoF (linear-angular) microsystem," in *Proc. IEEE Int. Conf. Robot. Autom. (ICRA)*, Orlando, FL, May. 15–19, 2006, pp. 669–674.

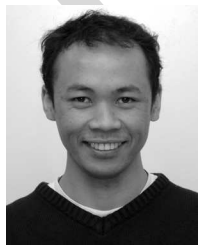

Micky Rakotondrabe (M'xx) received the Diploma in engineering from the Institut Supérieur de Technologie [IST-Institut Catholique des Arts et Métiers (ICAM)], Lille, France, in 2002, the D.E.A. Diploma (M.Sc. equivalent) in automatic control from the Institut National des Sciences Appliquées (INSA), Lyon, France, in 2003, and the Ph.D. degree in automatic control from the Université de Franche-Comté, Besançon, France, in 2006.

Since September 2007, he has been an Associate Professor at the Université de Franche-Comté, where he is also a Researcher at the Franche-Comté Electronique Mécanique Thermique et Optique–Sciences et Technologies (FEMTO-ST) Institute. His current research interests include modeling, control, and signal estimation in microsystems, especially based on piezoelectric materials.

Yassine Haddab received the Engineering degree in electrical engineering from the University of Tizi-Ouzou, Tizi-Ouzou, Algeria, the M.S. degree from the National School of Mechanics and Microtechnology (ENSMM), Besançon, France, and the Ph.D. degree from the University of Franche-Comté, Besançon, in 2000.

He was engaged in the design, the modeling, and the control of micromanipulation systems. Since 2002, he has been an Associate Professor at ENSMM, where he teaches control theory and microrobotics. His current research interests include design and control of high-precision microrobots and microsystems. He also contributes to the development of microfactory concepts and new microrobots architectures.

Philippe Lutz (M'xx) was an Engineer at the National School of Mechanics and Microtechnology (ENSMM) in 1990. From 1994 to 2002, he was an Associate Professor at the National Institute of Applied Science (INSA), Strasbourg, France, where he led the mechatronics activities and developed research on inventive theory for solving problems. In 2002, he joined the University of Franche-Comté, Besançon, France, as a Professor, where he was a Doctor in automation and computer science in 1994, and is currently the Head of the Automated Systems for Micromanipulation and Micro-Assembly, Department of Automatic Control and Micro-Mechatronic Systems (AS2M), Franche-Comté Electronique Mécanique Thermique et Optique–Sciences et Technologies (FEMTO-ST). His current research interests include design and the control of micromechatronic systems. He teaches at the master level the design of mechatronic systems and production system.